

Journal Pre-proofs

Role of Particle Size on the Multicycle Calcium Looping Activity of Limestone for Thermochemical Energy Storage

Jonatan D. Durán-Martín, Pedro E. Sánchez Jimenez, José M. Valverde, Antonio Perejón, Juan Arcenegui-Troya, Pablo García Triñanes, Luis A. Pérez Maqueda

PII: S2090-1232(19)30166-3
DOI: <https://doi.org/10.1016/j.jare.2019.10.008>
Reference: JARE 723

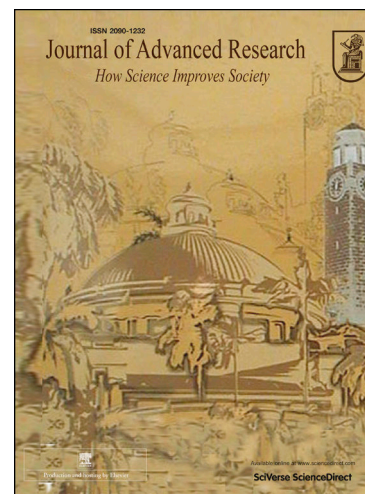
To appear in: *Journal of Advanced Research*

Received Date: 5 July 2019
Revised Date: 6 October 2019
Accepted Date: 21 October 2019

Please cite this article as: Durán-Martín, J.D., Sánchez Jimenez, P.E., Valverde, J.M., Perejón, A., Arcenegui-Troya, J., García Triñanes, P., Pérez Maqueda, L.A., Role of Particle Size on the Multicycle Calcium Looping Activity of Limestone for Thermochemical Energy Storage, *Journal of Advanced Research* (2019), doi: <https://doi.org/10.1016/j.jare.2019.10.008>

This is a PDF file of an article that has undergone enhancements after acceptance, such as the addition of a cover page and metadata, and formatting for readability, but it is not yet the definitive version of record. This version will undergo additional copyediting, typesetting and review before it is published in its final form, but we are providing this version to give early visibility of the article. Please note that, during the production process, errors may be discovered which could affect the content, and all legal disclaimers that apply to the journal pertain.

© 2019 THE AUTHORS. Published by Elsevier BV on behalf of Cairo University.



Role of Particle Size on the Multicycle Calcium Looping Activity of Limestone for Thermochemical Energy Storage

Jonatan D. Durán-Martín ^{*a}, Pedro E. Sánchez Jimenez ^{*a}, José M. Valverde ^b, Antonio Perejón ^c, Juan Arcenegui-Troya ^a, Pablo García Triñanes ^d and Luis A. Pérez Maqueda ^a

^a Instituto de Ciencia de Materiales de Sevilla, C.S.I.C.-Universidad de Sevilla, C. Américo Vespucio nº49, 41092 Sevilla, Spain.

^b Faculty of Physics, University of Seville, Avenida Reina Mercedes s/n, Sevilla, Spain.

^c Departamento de Química Inorgánica, Facultad de Química, Universidad de Sevilla, Sevilla, Spain.

^d Flow, Heat and Reaction Engineering Group, FHRENG, Chemical Engineering Division, School of Engineering, University of Greenwich, United Kingdom.

Role of Particle Size on Limestone Multicycle Activity

*Corresponding authors: Tel.:+34 954489576
email addresses: jonatan.duran@icmse.csic.es, pedro.enrique@icmse.csic.es

ABSTRACT

The calcium looping process, based on the reversible reaction between CaCO_3 and CaO , is recently attracting a great deal of interest as a promising thermochemical energy storage system to be integrated in Concentrated Solar Power plants (CaL-CSP). The main drawbacks of the system are the incomplete conversion of CaO and its sintering-induced deactivation. In this work, the influence of particle size in these deactivation mechanisms has been assessed by performing experimental multicycle tests using standard limestone particles of well-defined and narrow particle size distributions. The results indicate that CaO multicycle conversion benefits from the use of small particles mainly when the calcination is carried out in helium at low temperature. Yet, the enhancement is only significant for particles below $15\ \mu\text{m}$. On the other hand, the strong sintering induced by calcining in CO_2 at high temperatures makes particle size much less relevant for the multicycle performance. Finally, SEM imaging reveals that the mechanism responsible for the loss of activity is mainly pore-plugging when calcination is performed in helium, whereas extensive loss of surface area due to sintering is responsible for the deactivation when calcination is carried out in CO_2 at high temperature.

KEYWORDS

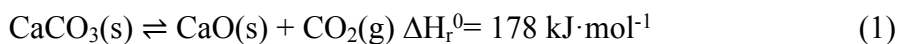
Concentrated Solar Power; Calcium Looping; Energy Storage; Calcium Oxide; Calcium Carbonate

Introduction

Global warming is one of the main challenges faced in this 21st century. The main cause is CO₂ emissions from anthropogenic origin, which are mainly produced by the combustion of fossil fuels [1]. Despite increasing effort in developing environmentally friendly technologies based on renewable energy sources, fossil fuel power plants still account for a significant share of the overall energy mix. Thus, greenhouse gas emissions from this type of facilities are still at unacceptable levels [2]. The main alternative renewable energy sources to replace fossil fuel power plants are wind and solar. Nonetheless, these technologies share an important shortcoming in their inability to provide a constant energy supply due to the intrinsic intermittency of wind and sunlight. Concentrated solar power plants (CSP) offer the possibility of integrating grid energy production with large-scale thermal energy storage (TES) thereby achieving dispatchability [3, 4]. TES systems in commercial CSP plants include steam accumulators and high specific heat molten salts [4-6]. However, storing the heat produced by direct solar radiation as chemical energy entail several advantages [7, 8]. For instance, the long-term storage of the products without radiative heat losses becomes possible. At the same, the continuous energy consumption required to maintain the salts in molten state is avoided [9]. Finally, Current molten salts are limited to about 560 °C to avoid degradation, thereby limiting the maximum attainable efficiency [10]. Achieving higher temperatures could boost the efficiency of the thermodynamic power cycle as the difference between charge and discharge temperature becomes larger [8, 11]. Finally, exergy efficiency is enhanced due to the larger energy densities provided by reaction enthalpies as compared to sensible and latent heats [8, 12, 13]. Among several chemical looping alternatives, the calcium looping (CaL) process has attracted a great deal of interest as a very promising system for thermochemical energy storage (TCES) since it displays several advantages

such as low cost, high reaction temperature, acceptable reversibility and high energy density [14-16].

In the last decades, the CaL process has been explored as an avenue to mitigate CO₂ emissions in fossil fuel power plants and cement manufacture facilities since it constitutes an effective technology for CO₂ capture and storage (CCS). The CaL process is based on the reversible calcination of CaCO₃ into CaO [17]:



This reaction has been widely studied since it is a fundamental step in cement production. Thus, it is relatively feasible to establish the optimum conditions for direct and reverse reaction depending on the application. CaCO₃ is inexpensive and abundant in the form of different minerals (limestone, marble, dolomite, etc) [18, 19]. It exhibits a high reaction enthalpy that allows for a high theoretical energy density, ranging from 1 to 4 GJ/m³ depending on the author and estimation method [12, 13, 20]. In the last years, several schemes regarding the integration of the CaL process in CSP plants (CaL-CSP) [14, 21-23]. These contemplate the calcination of CaCO₃ using direct solar radiation as heat source. Solar radiation can impinge directly on the storage material or it can be used to heat up the external walls of a solar particle receiver [14, 24]. Stored energy is recovered through the reverse exothermic solid-gas reaction between CaO and CO₂ at higher temperatures in the carbonator. Excess CO₂ out of the carbonator is then circulated to power a CO₂ turbine and produce electricity on demand. The high temperature of the working gas would ensure higher efficiency as compared with that of TES plants [16].

The CaL process exhibits two significant drawbacks that penalize its large-scale implementation, the incomplete conversion of CaO and its progressive deactivation along the successive carbonation/calcination cycles [14, 25]. The decay in CaO conversion is

generally attributed to the extensive sintering and loss of surface area that occur at the high temperature and high CO₂ partial pressure required [26-28]. Moreover, it has been observed that, when calcination is carried out in inert gas, a blocking CaCO₃ layer rapidly forms on the CaO particles surface during the subsequent carbonation. This pore-plugging layer severely hinders further diffusion of CO₂ molecules and prevents achieving complete conversion [29-31]. Therefore, the optimum conditions for CSP storage would be those that maximize the discharge temperature in order to improve the efficiency of the thermodynamic cycle while avoiding excessive sorbent deactivation. Recent studies have shown that can be achieved by carrying out the calcination at the lowest possible temperature in inert gas, and the carbonation at the maximum attainable temperature in CO₂, normally about 950 °C [32, 33]. However, pressurized carbonation (at ~ 3 bars) would allow to further extend the maximum carbonation temperature [16, 34].

Being one of the relevant challenges to overcome towards making the CaL-CSP technology attractive at industrial level, a number of strategies have been devised to reduce CaO deactivation. Thus, it is well known that crystallinity [35], particle size [18, 36], morphology [37, 38] and the inclusion of additives [19, 39] have a strong influence on Ca-based multicycle performance. Regarding the impact of particle size, it has been observed that large or highly crystalline particles exhibit substantially slower decarbonation kinetics, thereby requiring higher temperatures for the complete regeneration of CaO in short residence times [40]. Additionally, carbonation in large particles is hindered by pore diffusion and pore-plugging [30, 41, 42]. On the other hand, small particles exhibits faster calcination at lower temperatures, what eventually results in improved long term recyclability [18]. Moreover, the use of small particles would facilitate the integration with solar energy and decrease the cost in materials for constructing the solar receiver [43]. However, small particles are difficult to handle in

industrial processes based on fluidised bed reactors. Trajectories and residence times of particles in cyclones strongly depend on their size while collection efficiency decays markedly for particles with sizes below 10 μm [44, 45]. Thus, the usual particle size lower limit to ensure an acceptable efficiency of cyclones is about 50 μm . Overall, the optimum particle size in pilot plants based on fluidised bed reactors has been found to lie within the 100–300 μm range [46, 47].

Despite its importance, the influence of particle size in CaL-CSP has yet to be explored in sufficient detail since most published works use material with very wide particle size distributions. In this study, multicycle CaL-CSP experiments have been carried out using limestone sample sets with well-defined particle sizes, ranging from small 4- μm particles to large 900- μm particles. At the same time, Scanning Electron Microscopy (SEM) has been used to observe the morphological changes undergone by the material during consecutive carbonation and calcination cycles, in order to assess the mechanism responsible of the loss of activity. The results herein shed light on the relationship between particle size, extent of conversion after each cycle and deactivation after repeated carbonation and calcination cycles. Two different CaL-CSP operation schemes have been considered. First, the calcination stage is carried out in helium (CSP-He) as originally conceived in [32]. This procedure takes advantage of the high thermal conductivity of helium and the high diffusivity of CO_2 in this gas to favour the calcination process so that full decarbonation is achieved in short residence times at temperatures as low as 700-750 $^\circ\text{C}$. However, employment of helium at industrial scale entails technical issues such as high cost, gas losses and the necessity of gas separation from CO_2 after calcination. Thus, the tests have also been carried out using an alternative operation scheme in CO_2 closed cycle. This second integration scheme would be less complicated to implement technically but would entail raising the calcination temperature up to 950 $^\circ\text{C}$.

Experimental

A. Materials

The samples used in this work were limestone from standard Eskal series supplied by KSL Staubtechnik GmbH (Germany). The Eskal series are widely used in powder technology studies as standards for calibration of equipment and testing. Particle size distributions were determined by laser diffraction as reported in [48]. Five different samples with a well-defined average particle size were studied (2, 4, 15, 30 and 80 μm). An additional sample with larger particle size, ranging from 700 to 1000 μm , was also tested. Samples will be referred hereafter as KO2, KO4, KO15, KO30, KO80 and KO900. PSD data are listed in Table 1 while frequency distributions of particle sizes for all samples are plotted in Fig. 1.

B. Methods

Multicycle calcination/carbonation tests were carried out in a TA instrument Q5000IR TG analyzer equipped with a IR furnace composed of a SIC reaction chamber heated by IR lamps that allows high cooling and heating rates up to $300\text{ }^{\circ}\text{C}\cdot\text{min}^{-1}$. Such rates are necessary to emulate realistic CaL conditions in which the material is rapidly circulated between carbonator and calciner at different temperatures. All tests were run using small sample masses ($\approx 10\text{ mg}$) in order to avoid interfering mass and heat transfer phenomena as well as to facilitate exchanges with the surrounding atmosphere. The reaction chamber has a volume of just 20 cm^3 . According to process simulations, the maximum efficiency in CaL-CSP plants, not considering pressurized conditions, is achieved when the carbonation reaction takes place in a high CO_2 concentration environment at about 850

°C [16]. Considering this, the samples were tested according to the energy storage conditions described below:

1. CSP-He

CSP-He experiments begin with a calcination step (from room temperature to 750 °C at 300 °C·min⁻¹) under He atmosphere followed by a 5-minute isothermal stage. After this first calcination, carbonation is initiated in pure CO₂ atmosphere by increasing the temperature at a rate of 300 °C·min⁻¹ up to 850 °C, and keeping this temperature for 5 min. Then, a new calcination stage is triggered by reducing the temperature at 300 °C·min⁻¹ down to 750 °C under He, followed by 5-minute isotherm. An intermediate step is introduced after calcination by decreasing the temperature down to 300 °C under He for 2 min. This stage is intended to simulate the extraction of sensible heat from reaction products after calcination. After this cooling step a new cycle is started, for a total of 20 carbonation/calcination cycles.

2. CSP-CO₂

CSP-CO₂ experiments begin with a precalcination stage (from room temperature to 950 °C at 300 °C·min⁻¹, held for 5 min) in high CO₂ concentration (95% CO₂/5% air vol/vol). Precalcination is followed by a carbonation stage without changing the atmosphere by quickly decreasing the temperature down to 850 °C at 300 °C·min⁻¹ and maintaining this temperature for 5 min. A total of 20 carbonation/calcination cycles were run in these tests.

SEM micrographs of gold-sputtered samples (40 mA, 30 s) were taken employing a Hitachi S4800 FEG microscope at 5 kV.

Nitrogen adsorption–desorption isotherms were measured using an ASAP2420 (Micromeritics) instrument. Samples degassing was carried out at 300 °C for 2 h. Total surface areas (S_{BET}) were determined using the BET equation. In order to prepare the amount of sample needed for BET measurements, a tubular furnace was employed. Samples were prepared in small batches (300 mg of CaCO_3 at a time) to minimize mass and heat transfer phenomena during the calcination and carbonation reactions. The experimental schemes were similar to that described in B.1 and B.2 but calcination times had to be extended to 30 minutes to ensure complete decarbonation.

Results and discussion

A. Multicycle conversion

Fig. 2 shows, as an example, the complete thermograms recorded in the multicycle tests in both CSP-He and CSP- CO_2 conditions for the KO30 sample. The main implication of the latter conditions is that calcination temperature needs to be raised up to 950 °C in order to achieve complete decarbonation within the scheduled 5-minute step, as compared to just 750 °C required when helium is used as carrier gas. Fig. 3 includes a detail of the 1st, 10th and 20th cycles, highlighting the differences in the fast kinetic-driven and diffusion driven carbonation phases depending on particle size and operation scheme. It has been amply reported that the carbonation in CaL processes proceeds through two well differentiated stages [42]; first a rapid reaction controlled phase that depends on CaO available surface which is abruptly followed by a much slower diffusion controlled phase that triggers once a barrier layer composed of CaCO_3 product forms, hindering further diffusion of CO_2 molecules [49]. The diffusion controlled stage becomes rate-limiting

step once the CaCO_3 product layer reaches the critical value that depends on reaction conditions [31].

Fig. 3 illustrates the influence of particle size, cycle number and operation scheme on the relative importance of fast reaction-controlled and slow diffusion-controlled carbonation stages. It can be inferred from the plots in Fig. 3a and 3b that in CSP-He the carbonation reaction is mainly determined by the fast reaction regime, with negligible CO_2 uptake during the subsequent diffusion-controlled stage. This behaviour serves to highlight the pore-plugging phenomenon, since the rapid formation of a blocking CaCO_3 layer limits further CO_2 diffusion to the porous interior of the particle. Therefore, in CSP-He conditions, the conversion at each cycle depends mostly on the extension of the carbonation achieved during the fast stage since the relative contribution of diffusion-controlled carbonation is very small. In contrast, the relative contribution of each carbonation phase differs in CSP- CO_2 . As shown in Fig. 3c and 3d, in CSP- CO_2 the weight of diffusion-controlled carbonation is much more relevant. The extension of the reaction-controlled stage during the first recarbonation is roughly independent of the particle size save for the largest KO900 particles, which displays an unusual behaviour that might be related to its substantially slower decarbonation kinetics. However, the diffusion-controlled regime is promoted in smaller particles. Finally, Fig. 3d shows a marked decrease of the reaction-controlled carbonation with the cycle number. After 10 cycles, the carbonation is mainly diffusive, what implies that the CaO is heavily sintered (Fig. 3d). Another important issue, illustrated in Fig. 4, is decarbonation kinetics. The measured reaction rate is much faster when calcining at CSP- CO_2 conditions due to the higher employed temperatures.

The CaO conversion (X) is used to quantitatively compare the performance of different materials and reaction conditions. This parameter provides a measure of the extension of

the reaction at any given cycle. It is defined as the ratio of the mass of CaO converted in the carbonation stage of each cycle to the total CaO mass before carbonation [50]. In order to extrapolate at long term and determine the residual conversion after a large number of cycles, the conversion plots can be fitted by the following semi-empirical equation [26, 50]:

$$X_N = Xr + \left(\frac{X_1}{K(N-1) + \left(1 - \frac{Xr}{X_1}\right)^{-1}} \right) \quad (2)$$

where Xr is the residual conversion, which converges asymptotically after a large number of cycles), K is the so-called deactivation constant, X_1 is the conversion at the first cycle and X_{20} the conversion at the 20th cycle. Best fitting parameters are included in Table 2. In summary, the data show that conversion achieved in CSP-He is in all cases higher than the conversion achieved in CSP-CO₂. However, the difference in residual conversion, the really relevant parameter for industrial purposes, is only significant for KO2 and KO4; the two smaller particle sizes tested.

Fig. 5 includes the comparison of the CaO conversion as a function of the cycle number obtained for each particle size and for both CSP-He and CSP-CO₂ reaction conditions. The largest particle size tested (KO900) in CSP-He conditions displays a low conversion during the first carbonation. That occurs because the first calcination is incomplete since decarbonation kinetics are very slow for such large particle sizes [30]. As expected, the decay of CaO conversion is more pronounced for larger particles since they are more liable to deactivation by pore-plugging [30]. Also, cycling stability is noticeably impaired in CSP-CO₂ due to the significantly harsher calcination conditions (950 °C in pure CO₂) thereby favouring the loss of reactive surface due to sintering [27]. However, the detrimental effect of using large particles is much more important in CSP-He, with a substantial drop in residual conversion from 0.55 to 0.15 as the average particle size (d_{50})

increases from 2 to 900 μm respectively. On the other hand, the handicap of using large particles is less significant in CSP-CO₂ conditions. In such case, the residual CaO conversion drops from 0.17 to just 0.07 for the same average size increase (from 2 and 900 μm). It is nonetheless surprising the limited influence of particle size on conversion observed in CSP-He over a minimum threshold value. Thus, multicycle conversion performance only improves substantially for average sizes below 15 μm . This entails significant implications towards any prospective application at large scale. Since fine particles below 50 μm are cohesive and cannot be fluidised in practical applications and long term conversion of large particles is not significantly worse in CSP-CO₂ conditions, our work suggests the technically simpler closed CO₂ system might eventually be more advantageous, at least from the point of view of materials performance.

B. Influence of particle size and reaction conditions on sample morphology

In order to gain a better understanding of the influence of particle size on multicycle performance, the morphological changes undergone during carbonation and calcination stages have been studied by SEM. For comparative purposes, the samples KO2 and KO80 are chosen as representative of very small and large particles respectively. Fig. 6 includes the micrographs of as received limestone. The relatively large particles in KO80 sample appear as non-aggregated individual particles comprising a narrow distribution range. On the other hand, KO2 particles form larger aggregates due to cohesive forces, which for this size are much stronger than the particle weight [51]. In both cases, particles are constituted by well-defined crystals.

SEM micrographs in Fig. 7 shows comparative sequences of the morphological changes undergone by KO2 and KO80 particles during the CaL cycles carried out in CSP-He

conditions. The micrographs correspond to the CaO arising after the first calcination stage, the CaCO₃ formed in the subsequent recarbonation stage; the CaCO₃ formed after 20 cycles and finally the CaO after calcination in the 20th cycle.

1. CSP-He

KO2 sample, composed of small particles averaging 2 μm , forms sizable aggregates through the entire multicycle experiment. After just one calcination and carbonation stage (Figs. 7a and 7b respectively) the individual particles can still be distinguished whereas repeating cycles lead to the merging of neighbouring particles into large porous structures (Figs. 7c and 7d). This morphology, composed of small aggregates, grants the material a remarkable cycling stability. Arguably, this structure proves very resistant to deactivation by pore-plugging, thereby ensuring a high surface area of CaO available for carbonation remains despite repeated cycling (Fig. 7d). In contrast, while KO80 particles leave a relatively porous structure after the initial carbonation (Fig. 7e), the subsequent carbonation stage leads to the rapid formation of a CaCO₃ blocking layer preventing the diffusion of CO₂ molecules to the interior of the particle. Subsequent calcination and carbonation stages eventually lead to the progressive sintering of the surface layer, which is ultimately the only part of the particle that undergoes repeated transformations. Fig 7g and 7h show the porous core underneath the sintered surface created by the pore-plugging effect after 20 calcination and carbonation cycles. The grain growth and sintering occur mainly during the carbonation stage as it is promoted by CO₂. Actually, both KO2 and KO80 samples (Figs. 7b and 7f) evidence considerable grain growth even after the first recarbonation, with the formation of a mosaic structure, comprised of about 1 micron grains covering the entire particle surface. Therefore, the limited grain size observed

underneath the external sintered layer in Fig 7g and 7h proves the inner core has remained inactive during the cycles. In the inset of Fig. 7h, a fracture is shown to emphasize the marked differences between the surface CaCO_3 shell and the inner unreacted CaO core. It should be noted that the inset in Fig. 7h was taken using identical magnification as the main image to better highlight the disparity in grain sizes. Finally, it is interesting how the conversion of CaCO_3 into CaO exhibits a shape-memory feature; the shades of the previous CaCO_3 grains are apparent in subsequent CaO (Fig. 7g). This shape-memory feature preserves the blocking layer along the carbonation and calcinations cycles and facilitates further sintering, leading to the progressive decay in CaO conversion.

The relationship between these morphological transformations and the multicycle behavior described in Figure 5a is clear. The relevance of the *pore-plugging* effect depends on particle size; the larger the size, the higher the volume of material that remains inactive underneath the plugging layer. Hence the limited CaO conversion exhibited by the larger particle sizes in the multicycle tests. For smaller particles, a greater fraction of the material contributes to conversion each carbonation stage. Furthermore, the CaO arising from the calcination of the mosaic-like sintered structure shows a significant loss of surface porosity (Fig. 7g) with respect to the starting material (Fig 7a) leading to a decay in CaO conversion along ensuing cycles. Table 3 includes the BET surface area values measured for KO2 and KO80 samples after one calcination and after 5 carbonation and calcination cycles. As expected, there is a reduction in surface area because of sintering after a few cycles. Surface available for carbonation decreases about 30% in the case of the small KO2 particles whereas the reduction reaches 50% for the larger KO80 particles. That difference can be attributed to the formation of the sintered surface layer. It is also interesting that the surface area for all 4 samples studied is quite similar after the first calcination.

2. CSP-CO₂

As it will be discussed hereafter, sample behaviour is remarkably different when cycled in CSP-CO₂ conditions, due to the harsher calcination conditions; pure CO₂ and a high temperature of 950 °C. The overall effect on the multicycle conversion is a worsening of cycling performance with respect to CSP-He conditions, especially in the case of smaller particles. The sequence shown in Figs. 8a to 8d illustrate how small KO₂ particles cycled in CSP-CO₂ conditions endure progressive aggregation, eventually leading to the formation of a macroporous structure constituted of merged neighbouring grains. Also, while in CaCO₃ form, well developed grains in mosaic structures are clearly distinguished. However, the morphology of subsequent CaO exhibits striking features that contrast with what previously observed in CSP-He. Instead of preserving the mosaic structure attained by CaCO₃ grains in the preceding carbonation stage, CaO arising in CSP-CO₂ conditions constitutes a macroporous globular structure containing large channels. Moreover, no differences in morphology were observed between the surface and the interior of the particles. Thus, it seems that pore-plugging phenomenon is not that relevant in this CSP-CO₂ operation scheme as the formation of macroporous channels largely prevents the particles to be completely covered by the clogging carbonate layer. This arrangement is a consequence of the high temperatures attained, well over CaCO₃ Tamman temperature (about 500 °C), that strongly promote mass transfer by solid state diffusion [52]. That, coupled with the grain-growth promoting effect of CO₂ lead to extensive sintering all over the entire particle volume. In the case of samples with small average size, neighbouring particles merge as seen in Fig 8c and 8d. After 20 carbonation and calcination cycles, the loss of surface area is substantial as observed in the insets of Fig 8c and 8g. The surface of the CaO appears smooth (Figs. 8d and 8h) in contrast with the cracked surface evidenced in samples cycled in CSP-He (Figs. 7d and 7h). The

progressive loss of micro and mesoporosity in CaO formed under CSP-CO₂ after repeated cycling might explain the reduction in relative weight of the fast reaction-controlled carbonation in relation to the diffusion-controlled carbonation. Besides, as illustrated in Fig. 4, decarbonation rate is at least five times faster at 950 °C in CO₂ than at 750 °C in helium. Sudden release of occluded gases in short times within a high mobility matrix might induce the formation of a globular-like or foamy structure, as it has been observed in a somewhat different systems, such as the pyrolysis of rice husk to form SiO₂ [53]. Contrary to what occurs in the case of CSP-He, under CSP-CO₂ operation conditions there is little advantage in using small-sized particles since the extensive sintering and particle merging rapidly destroy the relatively open structure displayed in CSP-He (Fig. 7b and 7d). Table 3 also includes the BET surface area values measured for KO2 and KO80 samples after one calcination and after 5 carbonation and calcination cycles in these experimental conditions. As it occurred in the previous CSP-He conditions, the decline in surface area after 5 consecutive carbonation and calcination reactions is more marked in larger particles, amounting to 75% and 40% for KO80 and KO2 samples respectively.

Conclusions

In this work, the influence of particle size on limestone multicycle chemical looping conversion has been studied under operation conditions relevant for thermochemical energy storage applications. Experimental multicycle tests have been carried out using calcination in helium at relatively low temperatures and calcination at high temperatures in 100% CO₂. Limestone particles of well-defined and narrow particle size distributions have been employed in the analysis. When calcination is carried out in helium at low temperature, the CaO conversion is substantially better for small particles as they are more resilient to pore-plugging, the main deactivation mechanism in CSP-He. Nevertheless, the enhancement is only substantial for particles below 15 μm, which might

be difficult to employ in industrial applications involving fluidised bed reactors. Over that size, the formation of a blocking CaCO_3 layer on the particles surface prevents further diffusion of CO_2 to the inner particle core. Thus, a substantial volume of material remains inactive during the carbonation stage thereby limiting CaO conversion. On the other hand, when calcination is carried out in CO_2 at high temperatures, the deactivation of the material can be attributed to severe sintering all over the entire particle volume and the loss of surface porosity. Consequently, the improvement in conversion achieved by using particles with small average size is very limited. For particle sizes over $15\ \mu\text{m}$, the multicycle performance is relatively similar regardless the operation conditions. Thus, the CSP- CO_2 scheme of closed loop might be more advantageous for techno-economic reasons due to the high cost of helium and the simplicity of design. It has also been found that the carbonation process in CSP-He is mostly driven by fast kinetically controlled reaction while in CSP- CO_2 conditions solid-state diffusion has a relevant contribution. The residual CaO conversion attained in our experiments for particle-size usable at industrial level is still below 0.4, the critical value to make the technology competitive with respect to molten salts. Nevertheless, the sequence of morphological changes here presented brings valuable insight into the deactivation mechanism and can provide researchers a guide regarding the type of macroporous structures to be sought in order to minimise the sorbent deactivation.

Acknowledgements

AP thanks financial support from VI PPIT-US and VPPI-US for his current contract. PSJ is supported by a Ramón y Cajal Grant provided by the Ministerio de Economía y Competitividad. We also acknowledge the funding received by the European Union's

Horizon 2020 research and innovation programme under grant agreement No 727348, project SOCRATCES.

References

1. Jiang, X. and D. Guan, *Determinants of global CO₂ emissions growth*. Applied Energy, 2016. **184**: p. 1132-1141.
2. Su, M., et al., *Greenhouse gas emission accounting for EU member states from 1991 to 2012*. Applied Energy, 2016. **184**: p. 759-768.
3. Pietzcker, R.C., et al., *Using the sun to decarbonize the power sector: The economic potential of photovoltaics and concentrating solar power*. Applied Energy, 2014. **135**: p. 704-720.
4. Fernández, A.G., et al., *Mainstreaming commercial CSP systems: A technology review*. Renewable Energy, 2019. **140**: p. 152-176.
5. Weinstein, L.A., et al., *Concentrating Solar Power*. Chemical Reviews, 2015. **115**(23): p. 12797-12838.
6. Chen, X., et al., *State of the art on the high-temperature thermochemical energy storage systems*. Energy Conversion and Management, 2018. **177**: p. 792-815.
7. Pardo, P., et al., *A review on high temperature thermochemical heat energy storage*. Renewable and Sustainable Energy Reviews, 2014. **32**(Supplement C): p. 591-610.
8. Carrillo, A.J., et al., *Solar Energy on Demand: A Review on High Temperature Thermochemical Heat Storage Systems and Materials*. Chemical Reviews, 2019. **119**(7): p. 4777-4816.
9. Bonk, A., et al., *Advanced heat transfer fluids for direct molten salt line-focusing CSP plants*. Progress in Energy and Combustion Science, 2018. **67**: p. 69-87.
10. Fernández, Á.G. and L.F. Cabeza, *Molten salt corrosion mechanisms of nitrate based thermal energy storage materials for concentrated solar power plants: A review*. Solar Energy Materials and Solar Cells, 2019. **194**: p. 160-165.
11. Liu, M., et al., *Review on concentrating solar power plants and new developments in high temperature thermal energy storage technologies*. Renewable and Sustainable Energy Reviews, 2016. **53**: p. 1411-1432.
12. André, L., S. Abanades, and G. Flamant, *Screening of thermochemical systems based on solid-gas reversible reactions for high temperature solar thermal energy storage*. Renewable and Sustainable Energy Reviews, 2016. **64**(Supplement C): p. 703-715.
13. Prieto, C., et al., *Review of technology: Thermochemical energy storage for concentrated solar power plants*. Renewable and Sustainable Energy Reviews, 2016. **60**: p. 909-929.

14. Ortiz, C., et al., *The Calcium-Looping (CaCO₃/CaO) process for thermochemical energy storage in Concentrating Solar Power plants*. Renewable and Sustainable Energy Reviews, 2019. **113**: p. 109252.
15. Teng, L., et al., *Modified Ca-Looping materials for directly capturing solar energy and high-temperature storage*. Energy Storage Materials, 2019.
16. Chacartegui, R., et al., *Thermochemical energy storage of concentrated solar power by integration of the calcium looping process and a CO₂ power cycle*. Applied Energy, 2016. **173**(Supplement C): p. 589-605.
17. Blamey, J., et al., *The calcium looping cycle for large-scale CO₂ capture*. Progress in Energy and Combustion Science, 2010. **36**(2): p. 260-279.
18. Benitez-Guerrero, M., et al., *Multicycle activity of natural CaCO₃ minerals for thermochemical energy storage in Concentrated Solar Power plants*. Solar Energy, 2017. **153**(Supplement C): p. 188-199.
19. Erans, M., V. Manovic, and E.J. Anthony, *Calcium looping sorbents for CO₂ capture*. Applied Energy, 2016. **180**(Supplement C): p. 722-742.
20. Sunku Prasad, J., et al., *A critical review of high-temperature reversible thermochemical energy storage systems*. Applied Energy, 2019. **254**: p. 113733.
21. Tregambi, C., et al., *An experimental characterization of Calcium Looping integrated with concentrated solar power*. Chemical Engineering Journal, 2018. **331**: p. 794-802.
22. Chen, X., et al., *The role of sensible heat in a concentrated solar power plant with thermochemical energy storage*. Energy Conversion and Management, 2019. **190**: p. 42-53.
23. Astolfi, M., E. De Lena, and M.C. Romano, *Improved flexibility and economics of Calcium Looping power plants by thermochemical energy storage*. International Journal of Greenhouse Gas Control, 2019. **83**: p. 140-155.
24. Ho, C.K., *A review of high-temperature particle receivers for concentrating solar power*. Applied Thermal Engineering, 2016. **109**: p. 958-969.
25. Salaudeen, S.A., B. Acharya, and A. Dutta, *CaO-based CO₂ sorbents: A review on screening, enhancement, cyclic stability, regeneration and kinetics modelling*. Journal of CO₂ Utilization, 2018. **23**: p. 179-199.
26. Grasa, G.S. and J.C. Abanades, *CO₂ capture capacity of CaO in long series of carbonation/calcination cycles*. Industrial & Engineering Chemistry Research, 2006. **45**(26): p. 8846-8851.
27. Borgwardt, R.H., *Calcium oxide sintering in atmospheres containing water and carbon dioxide*. Industrial & Engineering Chemistry Research, 1989. **28**(4): p. 493-500.
28. Valverde, J.M., et al., *Role of looping-calcination conditions on self-reactivation of thermally pretreated CO₂ sorbents based on CaO*. Energy & Fuels, 2013. **27**(6): p. 3373-3384.
29. Alvarez, D. and J.C. Abanades, *Pore-size and shape effects on the recarbonation performance of calcium oxide submitted to repeated calcination/recarbonation cycles*. Energy & Fuels, 2005. **19**(1): p. 270-278.

30. Benitez-Guerrero, M., et al., *Large-scale high-temperature solar energy storage using natural minerals*. Solar Energy Materials and Solar Cells, 2017. **168**(Supplement C): p. 14-21.
31. Alvarez, D. and J.C. Abanades, *Determination of the critical product layer thickness in the reaction of CaO with CO₂*. Industrial & Engineering Chemistry Research, 2005. **44**(15): p. 5608-5615.
32. Sarrion, B., et al., *On the Multicycle Activity of Natural Limestone/Dolomite for Thermochemical Energy Storage of Concentrated Solar Power*. Energy Technology, 2016: p. n/a-n/a.
33. Sarrión, B., et al., *Role of calcium looping conditions on the performance of natural and synthetic Ca-based materials for energy storage*. Journal of CO₂ Utilization, 2018. **28**: p. 374-384.
34. Sarrion, B., et al., *Pressure Effect on the Multicycle Activity of Natural Carbonates and a Ca/Zr Composite for Energy Storage of Concentrated Solar Power*. ACS Sustainable Chemistry and Engineering, 2018. **6**(6): p. 7849-7858.
35. Biasin, A., C.U. Segre, and M. Strumendo, *CaCO₃ Crystallite Evolution during CaO Carbonation: Critical Crystallite Size and Rate Constant Measurement by In-Situ Synchrotron Radiation X-ray Powder Diffraction*. Crystal Growth & Design, 2015. **15**(11): p. 5188-5201.
36. Khinast, J., et al., *Decomposition of limestone: The influence of CO₂ and particle size on the reaction rate*. Chemical Engineering Science, 1996. **51**(4): p. 623-634.
37. Sánchez Jiménez, P.E., et al., *High-performance and low-cost macroporous calcium oxide based materials for thermochemical energy storage in concentrated solar power plants*. Applied Energy, 2019. **235**: p. 543-552.
38. Ma, X., et al., *Preparation of a morph-genetic CaO-based sorbent using paper fibre as a biotemplate for enhanced CO₂ capture*. Chemical Engineering Journal, 2019. **361**: p. 235-244.
39. Khosa, A.A. and C.Y. Zhao, *Heat storage and release performance analysis of CaCO₃/CaO thermal energy storage system after doping nano silica*. Solar Energy, 2019. **188**: p. 619-630.
40. Valverde, J.M., P.E. Sanchez-Jimenez, and L.A. Perez-Maqueda, *Relevant influence of limestone crystallinity on CO₂ capture in the Ca-Looping technology at realistic calcination conditions*. Environmental Science & Technology, 2014. **48**(16): p. 9882-9889.
41. Grasa, G.S., et al., *Reactivity of highly cycled particles of CaO in a carbonation/calcination loop*. Chemical Engineering Journal, 2008. **137**(3): p. 561-567.
42. Grasa, G., et al., *Application of the random pore model to the carbonation cyclic reaction*. AIChE Journal, 2009. **55**(5): p. 1246-1255.
43. Behar, O., A. Khellaf, and K. Mohammedi, *A review of studies on central receiver solar thermal power plants*. Renewable and Sustainable Energy Reviews, 2013. **23**(Supplement C): p. 12-39.
44. Zhao, B., Y. Su, and J. Zhang, *Simulation of gas flow pattern and separation efficiency in cyclone with conventional single and spiral double inlet*

- configuration*. Chemical Engineering Research and Design, 2006. **84**(12 A): p. 1158-1165.
45. Valverde, J.M. and M.A.S. Quintanilla, *Attrition of Ca-based CO₂-adsorbents by a high velocity gas jet*. AIChE Journal, 2013. **59**(4): p. 1096-1107.
 46. Arias, B., et al., *Demonstration of steady state CO₂ capture in a 1.7 MWth calcium looping pilot*. International Journal of Greenhouse Gas Control, 2013. **18**(0): p. 237-245.
 47. Strohle, J., et al., *Carbonate looping experiments in a 1 MWth pilot plant and model validation*. Fuel, 2014. **127**: p. 13-22.
 48. Shi, H., et al., *Effect of Particle Size and Cohesion on Powder Yielding and Flow*. KONA Powder and Particle Journal, 2018. **advpub**.
 49. Sun, Z., et al., *Ionic diffusion through Calcite (CaCO₃) layer during the reaction of CaO and CO₂*. Chemical Engineering Science, 2012. **81**(0): p. 164-168.
 50. Valverde, J.M., et al., *CO₂ multicyclic capture of pretreated/doped CaO in the Ca-looping process. Theory and experiments*. Physical Chemistry Chemical Physics, 2013. **15**(28): p. 11775-11793.
 51. Castellanos, A., J.M. Valverde, and M.A.S. Quintanilla, *Aggregation and sedimentation in gas-fluidized beds of cohesive powders*. Physical Review E, 2001. **64**(4): p. 041304.
 52. Merkle, R. and J. Maier, *On the Tammann-rule*. Zeitschrift für Anorganische und Allgemeine Chemie, 2005. **631**(6-7): p. 1163-1166.
 53. Vlaev, L.T., I.G. Markovska, and L.A. Lyubchev, *Non-isothermal kinetics of pyrolysis of rice husk*. Thermochimica Acta, 2003. **406**(1-2): p. 1-7.

LIST OF TABLES

Table 1. PSD data of limestone samples (adapted from [48])

Sample		KO2	KO4	KO15	KO30	KO80	KO900
Particle size (μm)	d_{10}	0.78	1.6	12	21	39	738
	d_{50}	2.22	4.42	19	30	71	938
	d_{90}	4.15	8.25	28	43	106	1148
Span	$(d_{90}-d_{10})/d_{50}$	1.52	1.50	0.84	0.73	0.94	0.44

Table 2. CaO conversion values (at 1st, 20th and residual conversion) and deactivation constants for limestone samples at CSP-He and CSP-CO₂ conditions. ΔX_r is the difference in residual conversions estimates for each particle size and conditions employed.

Sample	KO2		KO4		KO15		KO30		KO80		KO900	
Calcination Conditions	He	CO ₂	He	CO ₂	He	CO ₂	He	CO ₂	He	CO ₂	He	CO ₂

X_1	0.79 0.63	0.78 0.66	0.72 0.63	0.73 0.61	0.74 0.59	0.53 0.64
X_{20}	0.62 0.23	0.50 0.22	0.31 0.20	0.26 0.17	0.24 0.15	0.24 0.14
X_r	0.55 0.17	0.42 0.16	0.20 0.14	0.15 0.12	0.15 0.08	0.15 0.07
ΔX_r	0.38	0.26	0.06	0.03	0.07	0.08
K	0.37 0.44	0.37 0.41	0.29 0.48	0.30 0.56	0.42 0.41	0.32 0.56

Table 3. BET Surface area measured for KO2 and KO80 samples in CaO form after 1 calcination and after 5 carbonation/calcination cycles. Both CSP-He and CSP-CO₂ reaction conditions were tested.

Sample	S_{BET} (m ² /g)	
	1 calcination	5 carb/calc cycles
<u>KO2-He</u>	14.9	10.2
<u>KO2-CO₂</u>	11.3	6.8
<u>KO80-He</u>	16.3	8.5
<u>KO80-CO₂</u>	15.3	3.9

LIST OF FIGURE CAPTIONS

Figure 1. Frequency distributions of particle sizes (q3) measured for all tested samples.

Figure 2. Multicycle thermograms corresponding to KO30 sample in CaL tests carried out in (a) CSP-He and (b) CSP-CO₂ conditions.

Figure 3. Time evolution of temperature and mass % for the 1st calcination/carbonation cycle in (a) CSP-He and (c) CSP-CO₂ conditions for different particle sizes and comparison of 1st, 10th and 20th cycle for the KO80 sample in (b) CSP-He and (d) CSP-CO₂.

Figure 4. Comparison of the decarbonation rate of KO80 sample measured at the 4th cycle under both CSP-He and CSP-CO₂.

Figure 5. CaO conversion (**X**) as a function of the cycle number (**N**) for CaL tests of limestone of different particle sizes carried out at CSP-He (**a**) and CSP-CO₂ (**b**) conditions. Solid lines correspond to best fits of Eq. (2) to the experimental data

Figure 6. SEM micrographs illustrating starting (a) KO2 and (b) KO80 particles.

Figure 7. SEM micrographs illustrating morphology changes during carbonation and calcination cycles in CSP-He conditions for limestone samples KO2 and KO80. (a) KO2 CaO after first calcination; (b) KO2 CaCO₃ after the first recarbonation; (c) KO2 CaO after 20 cycles, (d) KO2 CaCO₃ after 20 cycles, (e) KO80 CaO after first calcination; (f) KO80 CaCO₃ after the first recarbonation; (g) KO80 CaO after 20 cycles and (h) KO80 CaCO₃ after 20 cycles.

Figure 8. SEM micrographs illustrating morphology changes during carbonation and calcination cycles in CSP-CO₂ conditions for limestone samples KO2 and KO80. (a) KO2 CaO after first calcination; (b) KO2 CaCO₃ after the first recarbonation; (c) KO2 CaO after 20 cycles, (d) KO2 CaCO₃ after 20 cycles, (e)

KO80 CaO after first calcination; (f) KO80 CaCO₃ after the first recarbonation;
(g) KO80 CaO after 20 cycles and (h) KO80 CaCO₃ after 20 cycles.

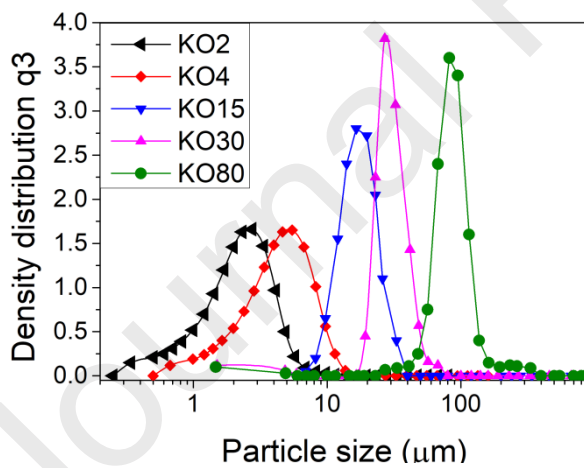
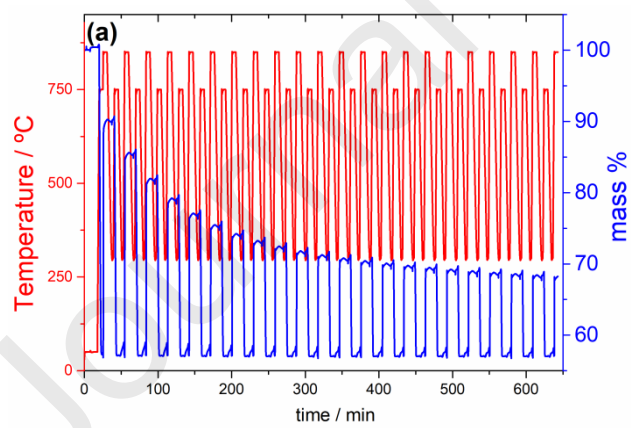


Fig. 1. Frequency distributions of particle sizes (q3) measured for all tested samples.



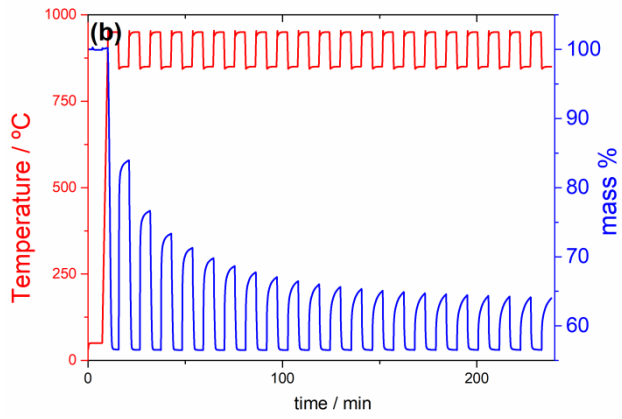


Fig. 2. Multicycle thermograms corresponding to [KO30](#) sample in CaL tests carried out in (a) CSP-He and (b) CSP-CO₂ conditions.

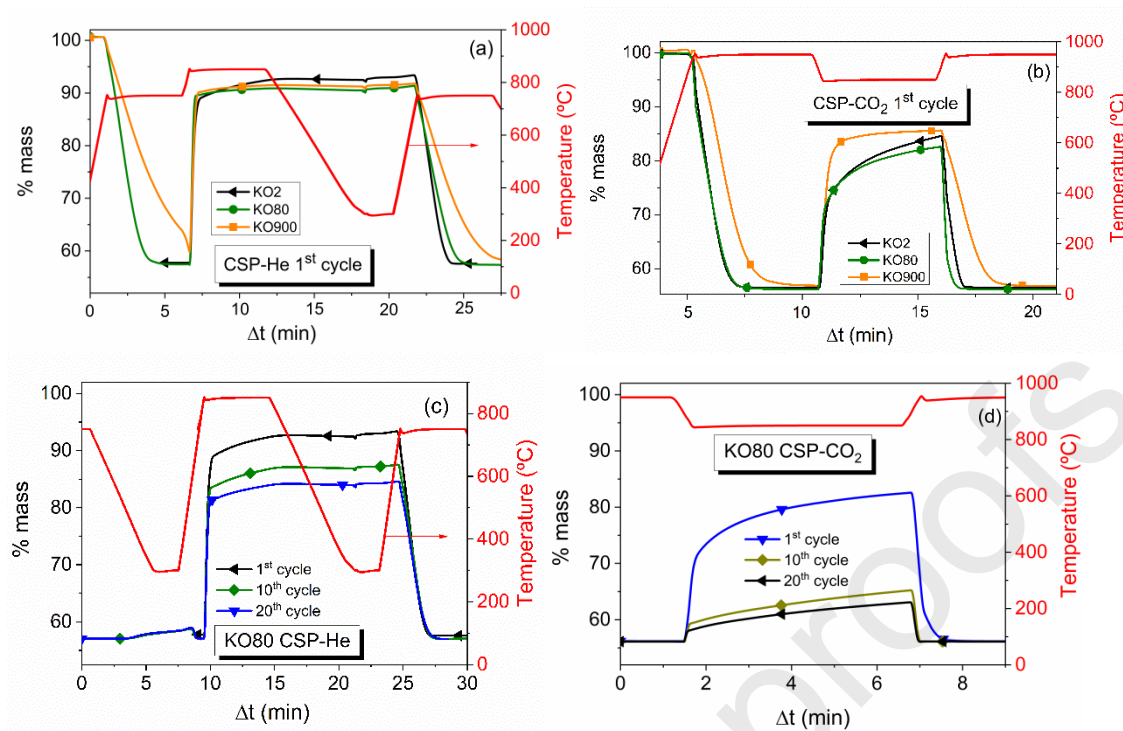


Fig. 3. Time evolution of temperature and mass % for the 1st calcination/carbonation cycle in (a) CSP-He and (b) CSP-CO₂ conditions for different particle sizes and comparison of 1st, 10th and 20th cycle for the KO80 sample in (c) CSP-He and (d) CSP-CO₂.

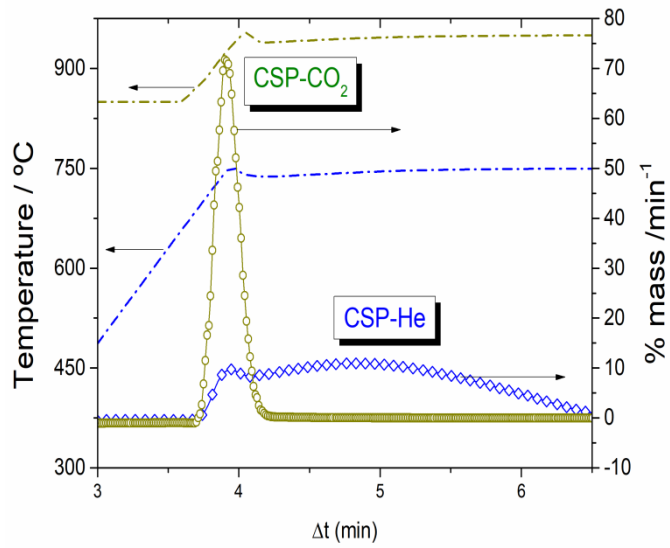


Fig. 4. Comparison of the decarbonation rate of KO80 sample measured at the 4th cycle under both CSP-He and CSP-CO₂.

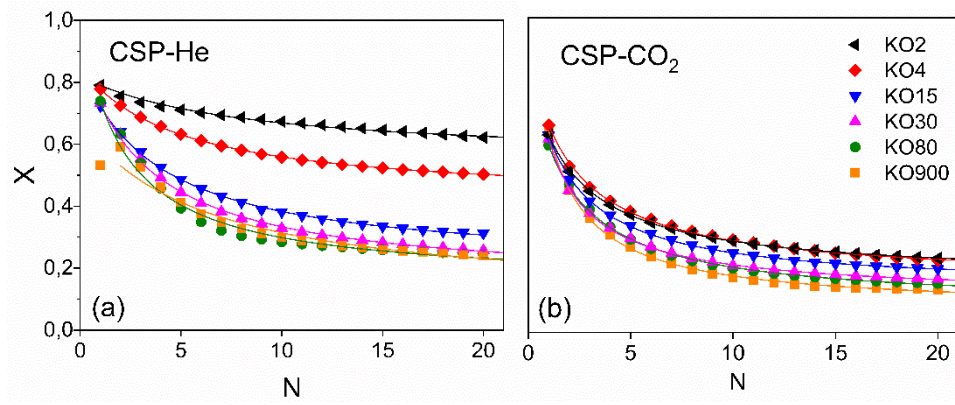


Fig. 5. CaO conversion (X) as a function of the cycle number (N) for CaL tests of limestone of different particle sizes carried out at CSP-He (a) and CSP-CO₂ (b) conditions. Solid lines correspond to best fits of Eq. (2) to the experimental data

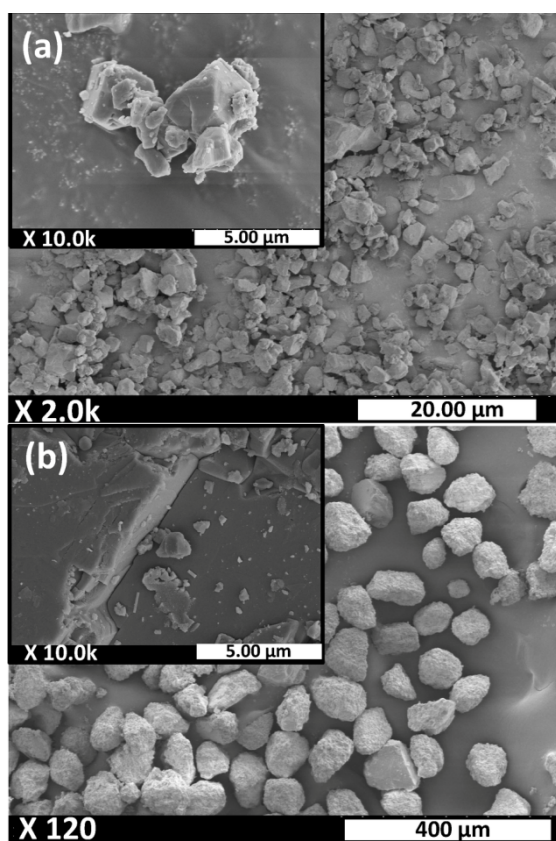


Fig. 6. SEM micrographs illustrating starting (a) KO₂ and (b) KO₈₀ particles.

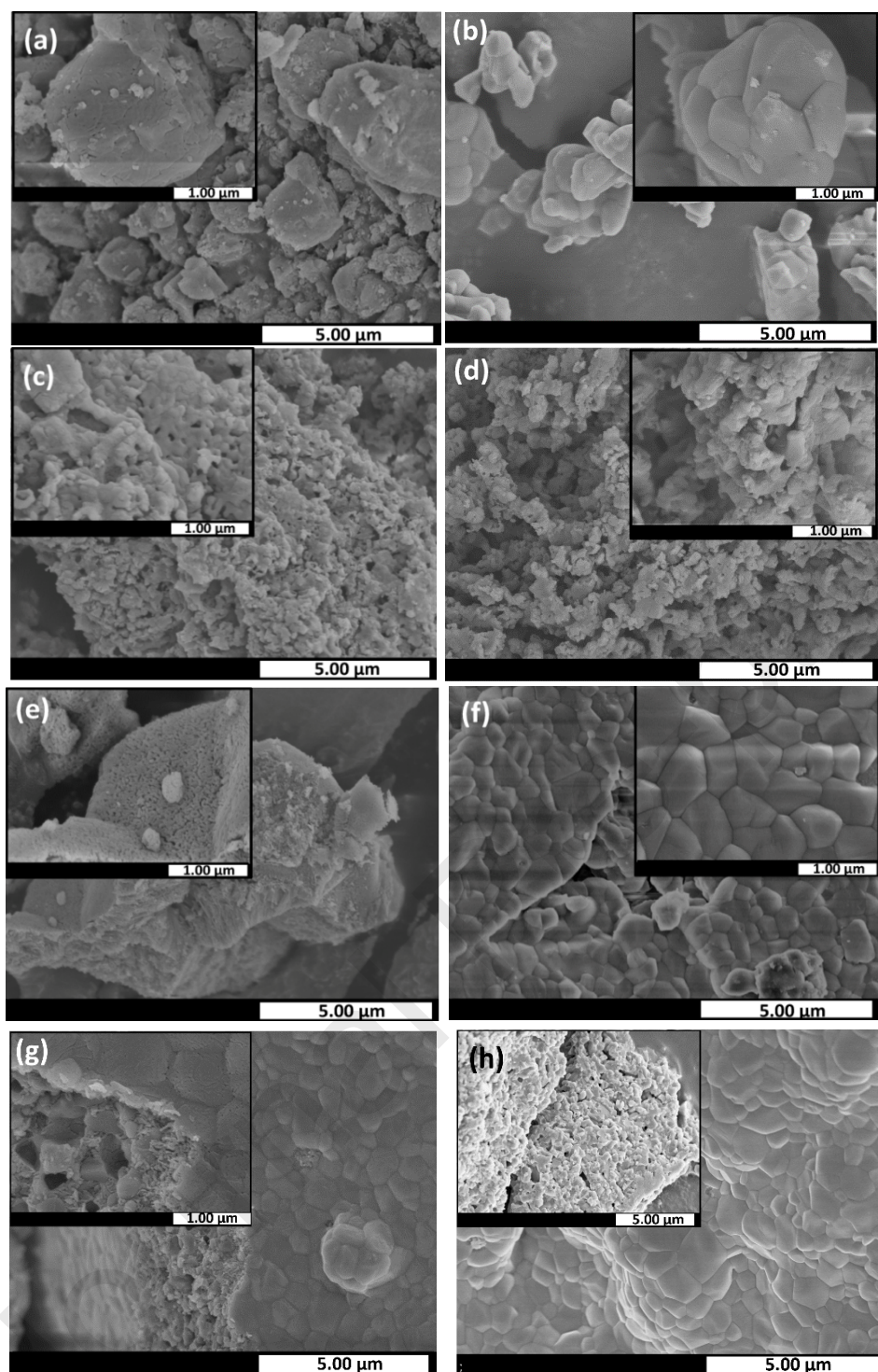


Fig. 7. SEM micrographs illustrating morphology changes during carbonation and calcination cycles in CSP-He conditions for limestone samples KO2 and KO80. (a) KO2 CaO after first calcination; (b) KO2 CaCO₃ after the first recarbonation; (c) KO2 CaO after 20 cycles, (d) KO2 CaCO₃ after 20 cycles, (e) KO80 CaO after first calcination; (f) KO80 CaCO₃ after the first recarbonation; (g) KO80 CaO after 20 cycles and (h) KO80 CaCO₃ after 20 cycles.

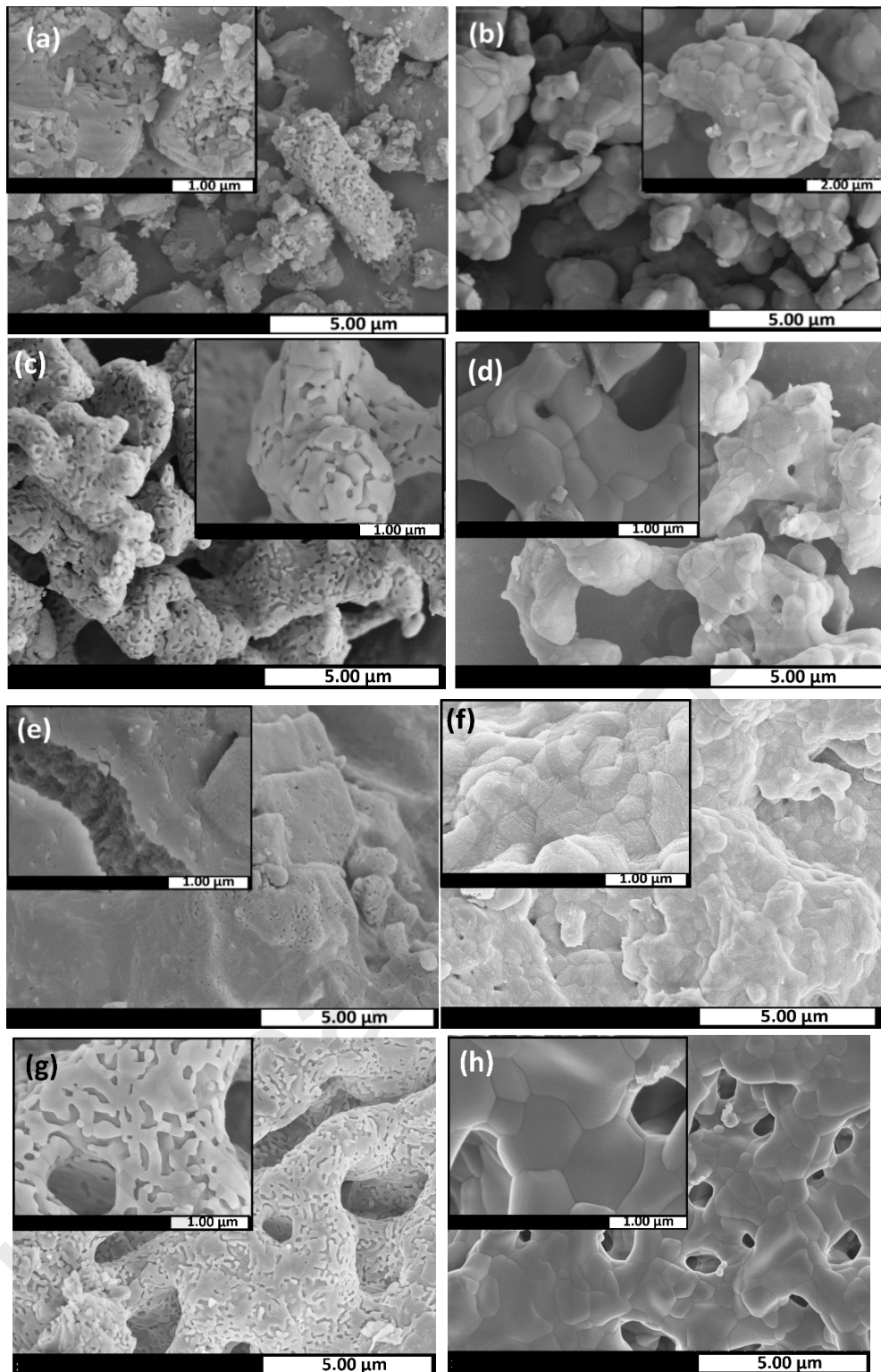
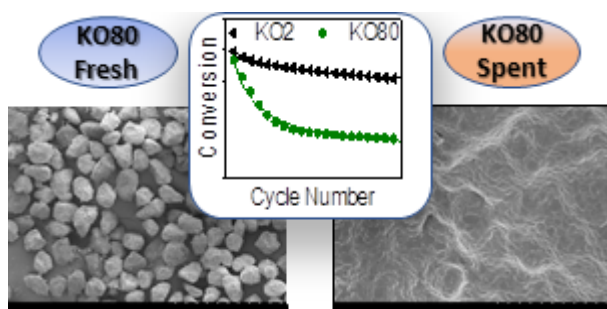


Fig. 8. SEM micrographs illustrating morphology changes during carbonation and calcination cycles in CSP-CO₂ conditions for limestone samples KO2 and KO80. (a) KO2 CaO after first calcination; (b) KO2 CaCO₃ after the first recarbonation; (c) KO2 CaO after 20 cycles, (d) KO2 CaCO₃ after 20 cycles, (e) KO80 CaO after first calcination; (f) KO80 CaCO₃ after the first recarbonation; (g) KO80 CaO after 20 cycles and (h) KO80 CaCO₃ after 20 cycles.

Graphical abstract



Compliance with Ethics Requirements

This article does not contain any studies with human or animal subjects

Journal Pre-proofs

Conflict of Interest

The authors have declared no conflict of interest

Journal Pre-proofs

Highlights

Thermal energy performance of narrow particle size distribution limestones is studied

Multicyclic activity is better for small particles under all the different studied conditions

This effect is particularly relevant for particles smaller than 15 μm median particle size.

Particle size effect is not relevant for particles between 15 and 900 μm .